Article

Modeling of Electrochemical Impedance of Fuel Cell Based on Novel Nanocomposite Membrane

Mariia Zhyhailo [1], Iryna Yevchuk [1], Fedir Ivashchyshyn [2,3,*], Oksana Demchyna [1], Piotr Chabecki [2], Natalia Babkina [4] and Tetiana Shantaliy [4]

[1] Department of Physical Chemistry of Fossil Fuels, Institute of Physical-Organic Chemistry and Coal Chemistry Named after L. M. Lytvynenko, National Academy of Sciences of Ukraine, Naukova Str. 3a, 79060 Lviv, Ukraine; zhygaylo@nas.gov.ua (M.Z.); irynayevchuk@gmail.com (I.Y.); demchynaoksana@ukr.net (O.D.)

[2] Faculty of Electrical Engineering, Czestochowa University of Technology, J. Dąbrowskiego Str. 69, 42-201 Czestochowa, Poland; piotr.chabecki@pcz.pl

[3] Institute of Applied Mathematics and Fundamental Sciences, Lviv Polytechnic National University, Bandera Str. 12, 79013 Lviv, Ukraine

[4] Institute of Macromolecular Chemistry NAS of Ukraine, Kharkivske Shaussee 48, 02160 Kyiv, Ukraine; nvbabkina@nas.gov.ua (N.B.); shantaliy@nas.gov.ua (T.S.)

* Correspondence: fedir.ivashchyshyn@pcz.pl or fedir.o.ivashchyshyn@lpnu.ua or fedirivashchyshyn@gmail.com

Abstract: The new hybrid composite materials for PEM fuel cell were synthesized by the UV polymerization of acrylic monomers (acrylonitrile, acrylic acid, ethylene glycol dimethacrylate) and a sulfo aromatic monomer, i.e., sodium styrene sulfonate, and the tetraethoxysilane/3-methacryloxypropyltrimethoxysilane-based sol–gel system. By means of X-ray spectroscopy, the fractal structure of the obtained materials was characterized. Proton conductivity and viscoelasticity of the obtained materials were determined depending on the content of the inorganic component in nanocomposites. Based on impedance studies, an equivalent scheme is proposed that successfully describes the proton conductivity in the synthesized composite's electrolyte membranes.

Keywords: fuel cell; impedance spectroscopy; Nyquist diagram; SAXS; proton conductivity; composite membrane

1. Introduction

Clean and efficient power is one of the sustainable development goals and a top priority for researchers. In recent years, fuel cells are regarded as a promising and eco-friendly technology with high reliability and broad development prospects [1,2]. It is important to note that gray hydrogen produced from fossil fuels is still not friendly to the environment, while green hydrogen produced from renewable energy by the electrolysis of water seems to be the best fuel for fuel cells. The implementation of renewable energy sources in fossil fuel replacement is not a simple task since these sources are as a rule intermittent, which creates spatial and temporal gaps between the availability and consumption of this energy [3]. Fuel cell power generation technology based on green hydrogen is a promising way to address these issues.

Proton-conductive membrane is the main element in fuel cell, determining its operating effectiveness and, therefore, must meet the following requirements: high proton conductivity, low permeability to fuel, good chemical and thermal stability, mechanical strength, and low cost. Nowadays, the Nafion (Du Pont) membranes (made of the perfluorosulfonic acid ionomer) are mainly used in fuel cell technology due to their excellent proton conductivity and high durability and chemical stability. At the same time, they are expensive and effective only at temperatures up to 90 °C [4]. Despite the fact that Nafion can operate at temperatures up to 120 °C, temperatures above 90 °C are much more likely

to present problems, since Nafion conductivity is related to the presence of water channels in hydrophilic domains; thus, it is inconvenient to operate Nafion below 0 °C and/or above 100 °C [5–7].

One more downside of the Nafion membrane is the necessity to use toxic chemicals during production. The chemical structure of Nafion consists of hydrophobic oroethylene (PTFE) backbone and side chains of hydrophilic sulfonic acid (-SO$_3$H), so it belongs to the group of per- and polyfluoroalkyl substances (PFASs). Fluorination is an expensive stage in the production of Nafion and similar PFASs [5]. The manufacture of PFASs poses a risk to human health and the environment. Fluorine-containing monomers have a toxic effect and can irritate the mucous membrane of the respiratory tract, eyes, and nasopharynx. The toxicity is explained by their ability to oxidize to unstable peroxide compounds that easily decompose when mixed with air with the formation of poisonous fluorophosgene. Fluorophosgene reacts with moist air and hydrolyzes when it hits the mucous membranes of the respiratory tract and lungs, resulting in the formation of hydrogen fluoride, which causes severe chemical burns.

The global concerns regarding PFASs' chemical and environmental effects are also connected with the production of toxic gases (COF$_2$, HF, etc.) when PFASs are thermally decomposed, and the inhalation of these gases leads to lung edema or inflammation. Under specific conditions, perfluorinated polymers produce toxic nanoparticles [8].

In order to introduce safe and ecofriendly technologies, the reduction of membrane cost and the expansion of the operating temperature range for proton-conductive membranes make their commercialization profitable; thus, scientists are taking efforts to develop such novel materials. Among the alternatives to Nafion, non-fluorinated membranes with aromatic structures have been developed [9,10]. Aromatic materials have good thermal and mechanical properties, tunable proton conductivities, and small methanol permeabilities, showing great potential to be used as PEMs [10].

The backbones of these polymers comprise aromatic or phenyl rings with varying number of ether, ketone, imide, or benzimidazole functionalities in their structures. Due to intramolecular interactions, sulfonated aromatic polymers (SAPs) possess film-forming properties. To provide proton conductivity to membranes, sulfonic acid groups (-SO$_3$H) are embedded on aromatic polymer chains through sulfonation reactions, producing sulfonated derivatives for application in PEMs [11–13]. Some common SAPs are sulfonated polyether ether ketone (SPEEK) [14], polyether sulfone (SPES) [15], and polyphenyl sulfone (SPPSU) [16].

To improve the properties of hydrocarbon-based PEMs, different methods have been applied by researchers, including the use of nanofillers. As a rule, introducing the inorganic blocks into the organic polymer matrix at the molecular level leads to the formation of inorganic/organic composite membranes that combine the properties of a mechanically and thermally stable inorganic network and chemical stability, flexibility, conductivity, and plasticity of an organic polymer.

The sol–gel technique is a convenient method for the introduction of inorganic nanoparticles into a polymeric matrix as it allows the in situ formation of nanoparticles during the polymerization process [17]. Since the materials for the synthesis of nanocomposites by the sol–gel method are in the liquid phase, the efficient homogenization of the system is achieved, and the obtained hybrid inorganic/organic materials are highly homogeneous. In the organic and inorganic components of the hybrid nanocomposites, the different types of bonds that can occur are as follows: hydrogen bonds, weak or strong covalent bonds, and ionic bonds. The compatibility between these two phases defines the physicochemical properties of the nanocomposite membranes, including proton conductivity.

To analyze and predict the fuel cell operating efficiency, the ionic conduction mechanism is modeled using appropriate electrical circuits [18–20]. Impedance spectroscopy is an effective method for investigating the charge transfer processes in fuel cells, providing the highest accuracy for a wide range of operating signal frequencies and extensive information about the properties of the object under study [21,22].

It is important to evaluate different voltage loss contributions. To achieve this goal, appropriate models are required. Cell impedance analysis and interpretation allow to determine the optimal operating conditions. They also make it possible to optimize the cell design [23]. Developments in this direction are hampered by the complexity of the processes in heterogeneous systems.

The aim of our work was to model the proton conducting behavior of the fuel cell with the new proton-conductive membranes developed on the basis of cross-linked organic/inorganic materials synthesized by the UV polymerization of acrylic monomers including aromatic monomers and sol–gel systems prepared from the precursors, e.g., TEOS/MAPTMS, and also to study the properties of the membranes.

2. Materials and Methods

Materials: Acrylonitrile (AN, 99%), acrylic acid (AA, 99%), sodium styrene sulfonate (SSS, 99%), ethylene glycol dimethacrylate (EGDMA, 99%), tetraethoxysilane (TEOS, 99%), 3-methacryloxypropyltrimethoxysilane (MAPTMS, 99%), photoinitiator 2,2-dimethoxy-2-phenylacetophenone (DMPA, 99%), and phosphoric acid (PhA, 85%) (Sigma-Aldrich, Darmstadt, Germany) were used without further purification. Milli-Q® water, absolute ethanol (VWR), and acetone (Analytical Grade, Fisher Scientific, Vantaa, Finland) were used as solvents.

Polymer and hybrid composite material syntheses: Proton-conductive polymer material was prepared via UV curing of the monomer mixture. Preparation procedure was as follows [24]: AA and SSS were dissolved in DW and then mixed with AN, EGDMA, and DMPA under stirring (500 rpm) till a homogeneous solution was formed. The resulting composition in a glass mold was exposed to UV irradiation (365 nm, 15 J·cm^{-2}) from the multi-lamp BIO-LINK® cross-linker (BLX-365, Witec AG, Sursee, Switzerland) equipped with 5 UV lamps (8 W, output 0.8 W) where polymerization process took place. Oxygen is known to be the inhibitor of polymerization, so air access was blocked by transparent covers. The cured films were separated from the molds and rinsed with the solvents. Finally, the materials were dried to a constant weight in an oven at 323 K.

The feed composition for the synthesis of a polymer matrix of the material was as follows (wt. %): AN—45; AA—20; EGDMA—20; and SSS—15. To obtain hybrid composite materials NSSA, NSSA/SG3, NSSA/SG5, NSSA/SG7, and NSSA/SG10, 0, 3, 5, 7, and 10 wt. % of the sol–gel system were added, respectively. The sol–gel procedure was similar to that described in [25], and TEOS and MAPTMS precursors, ethanol, distilled water, and orthophosphoric acid were mixed in the following ratio: TEOS:MAPTMS:C_2H_5OH:H_2O:H_3PO_4 = 0.75:0.25:4:4:1.2 (mol). Components were continuously stirred (500 rpm) at 323 K for 180–200 min until the mixture became homogeneous. When the sol–gel system was added to the monomer mixture and stirred (500 rpm), a homogeneous solution was formed. The procedure used after this step for preparing a hybrid inorganic/organic membrane was the same as in the case of the pure polymer membrane.

Characterization:

Small-Angle X-ray Scattering: SAXS measurements were carried out on Ganesha 300 XL+ instrument (SAXSLAB ApS, Denmark/USA) equipped with Pilatus 300K 2D-detector, with a pixel size of 172 × 172 mm^2. X-ray beam (0.1542 nm, a cross-section of 0.3 × 0.3 mm^2) from a monochromatic Cu-K$_a$ radiation source (l-focus tube, 50 kV, 600 mA, monochromatization with bifocal Göbel mirror) was used. During measurements, samples were wrapped in an Al foil. The distance from the sample to the detector was 1060 mm, which allows obtaining the scattering data in the *q*-range ca. 0.05–2.9 nm^{-1}. The scattering patterns were acquired for 3 h and radially averaged to obtain one-dimensional (1D) scattering intensity profiles. All scattering profiles were corrected for the scattering generated by the Al foil.

Proton conductivity: The conductivity of all synthesized materials was studied by impedance spectroscopy using the cell for the study of electrochemical systems shown in Figure 1. This is a stainless steel two-electrode split test cell for coin cell research (from China). For the study, the samples were cut into circles (d = 2 cm) and placed between

two steel electrodes, which were pressed with equal force by a spring located at the top of the cell. Before the measurement, the membranes were converted into an acidic form. For this, they were placed in 0.1 M HCl. Impedance spectra were measured using a measuring complex Autolab/FRA-2 (the Netherlands) at frequencies of $0.1–10^5$ Hz. The modeling of the impedance spectra in accordance with the equivalent electrical circuit was performed in the ZView2.3 software environment (Scribner Associates, Southern Pines, NC, USA).
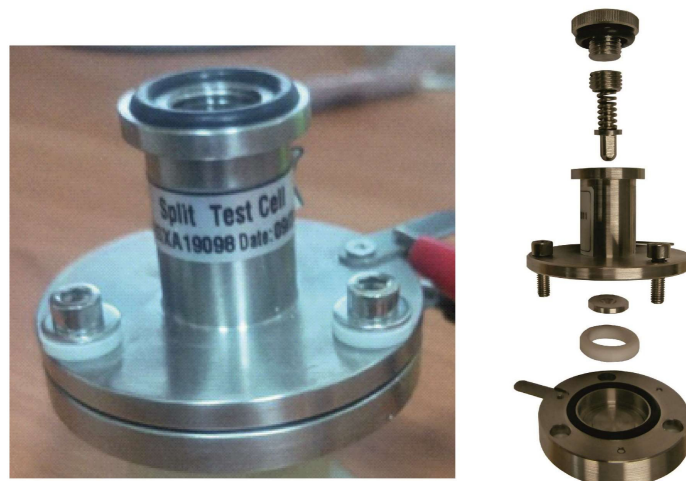

Figure 1. The cell in which the proton conductivity of the membrane was studied.

Dynamic mechanical analysis: To study the viscoelastic properties of the hybrid composite materials, DMA was performed using DMA Q800 (TA Instruments, New Castle, DE, USA) in the tensile mode at a frequency of 10 Hz. The experiments were carried out at 293-473 K, and the heating rate was 3 K/min.

3. Results

Feed composition for the hybrid material synthesis was chosen in a manner that it provided the resulting material the required properties. SSS contains the -SO_3H moiety in its structure, which dissociates in wet conditions to form a proton that moves through the material from anode to cathode. Additionally, SSS endows the polymer material with good mechanical and thermal properties [26]. AN is a commercially available and inexpensive monomer. A significant advantage of AN is excellent mechanical and film-forming properties. AA is also an available and inexpensive monomer with an ionic -COOH group that serves as an additional source of protons. EGDMA was used as a cross-linker. The MAPTMS precursor has an acrylate moiety that allows it to be incorporated into the polymer chain. At the same time, MAPTMS contains a methoxysilyl group that can be hydrolyzed to silanol [-$Si(OH)_3$] in an aqueous medium and condensed into a cross-linked silica network [25]. Thus, both organic and inorganic parts are joined in the hybrid material by chemical bonds. As the sol–gel transformation of MAPTMS slowly occurs, we changed a part of this precursor with TEOS. The amphiphilic structure of the obtained materials provides formed channels for proton transport.

Figure 2 shows the formation of the cross-linked hybrid composite material. A polymeric matrix was formed as a result of the UV-initiated copolymerization of acrylic monomers and SSS. DMPA was used as a photoinitiator. The sol of inorganic nanoparticles previously formed from sol–gel precursors was introduced into the polymerization composition before gelation. The process of gelation that forms the silica network takes place in situ simultaneously with the polymerization.
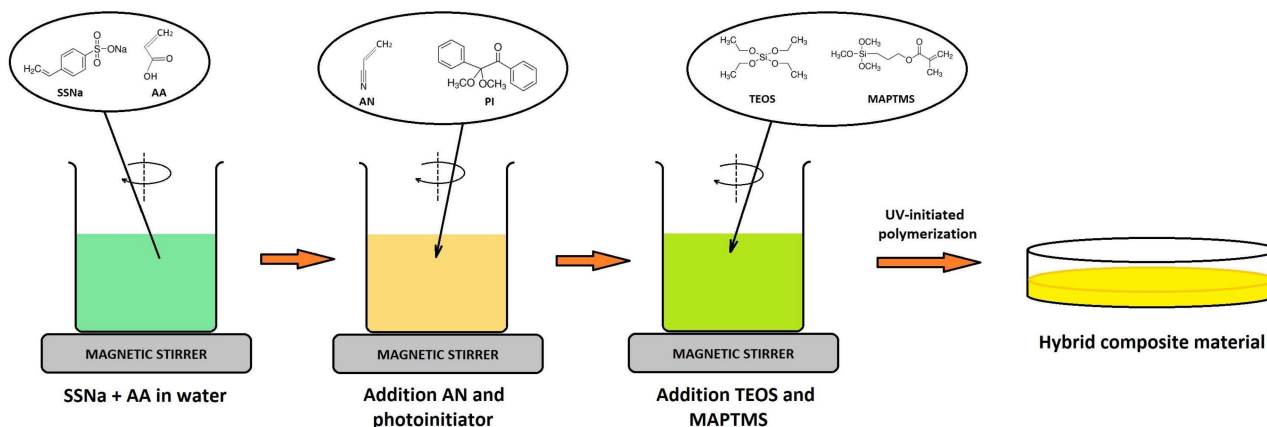
Figure 2. Scheme of the nanocomposite membrane synthesis.

It is known that the final properties of the hybrid composite material depend on its morphology. Therefore, we aimed to reveal and investigate influence of the sol–gel system on synthesized materials' morphology, and for this, the SAXS spectra for the hybrid materials, NSSA/SG3 and NSSA/SG10, were obtained (Figure 3).
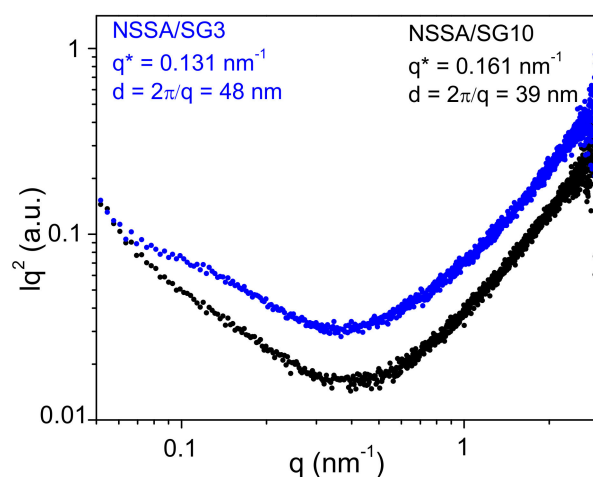

Figure 3. SAXS spectra of the composites NSSA/SG3 and NSSA/SG10 in coordinates I·q^2 = f(q).

In the dependence *I(q)* vs. *q* of the logarithmic coordinates, the Guinier region can be observed at very small angles. In this region, the following equation (Figure 3) is valid:

$$I(q) = G exp\left(\frac{-q^2 Rg^2}{3}\right),\qquad(1)$$

where *I(q)* is the scattering intensity, *G* is the Guinier scale factor, R_g is the radius of gyration, and *q* is Fourier spatial frequency or scattering vector:

$$q = 4\pi\sin\left(\frac{\theta}{2}\right)/\lambda\qquad(2)$$

where λ is the incident radiation wavelength.

Domain characteristic dimension d (d = $2\pi/q$) was calculated from the value of *q* (q = 0.131 nm^{-1} for NSSA/SG3 and 0.161 nm^{-1} for NSSA/SG10) (Table 1).

Table 1. SAXS data of the nanocomposite membranes.

Sample	R_g, nm	d, nm	D_f
NSSA/SG3	24	48	2.9
NSSA/SG10	20	39	2.7

The size of inorganic domain can be estimated by the radius of gyration, since R_g reflects mean square distance between inorganic domain scattering centers and the center of gravity. The value of R_g was calculated from the slope of the $\ln(I(q))$ vs. q^2 plot in the linear region (Figure 4, Table 1).
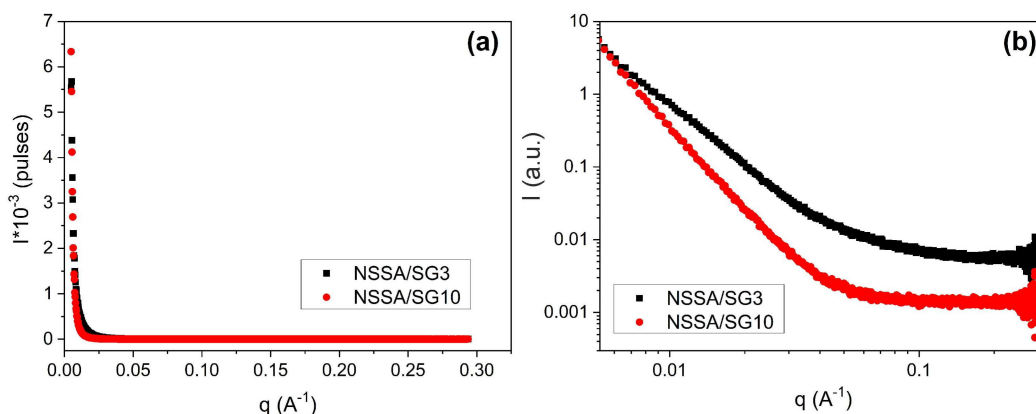
Figure 4. SAXS spectra of the composites NSSA/SG3 and NSSA/SG10: (**a**) initial; (**b**) in the double logarithmic coordinates.

The fractal dimensions D_f are low power exponents calculated using the slope of the linear part of the plot $log\ I(q) - log\ q$ (the so called Porod plot):

$$I(q) = q^{-\beta} \tag{3}$$

This parameter is the measure of the compactness of the material [26]. For the NSSA/SG3 and NSSA/SG10 membrane samples, the values of D_f were determined to be 2.9 and 2.7, respectively (Table 1). If the absolute value of $|\beta|$ is 1–3, fractal aggregates can be attributed to mass fractals, and $D_f = |\beta|$. This indicates the formation of massive fractals in our case.

For the exploitation of the membrane as a PEM for fuel cells, an important characteristic is its viscoelastic behavior. The temperature dependences of storage and loss moduli (E′ and E″, respectively) the and mechanical loss factor (tan δ) were determined using dynamic mechanical analysis (Figure 5).

Notably, the viscoelastic dependences of the polymeric NSSA membrane and the organic/inorganic NSSA/SG10 membrane are similar, as evidenced by the similar shape of the DMA curves, which reflects the phase morphology (Figure 5). For both membranes, two relaxation transitions are observed in the temperature range of 298–470 K, which indicate the two-phase structure of the obtained copolymers. These relaxation transitions are recorded as areas of a sharp decrease in the storage modulus for the temperature dependence of E′ (Figure 5a), with a maximum at T = 350 K and a shoulder in the region of 420–430 K for the temperature dependence of E″ (Figure 5b), and for the dependence of tan δ(T), as a pronounced shoulder at the temperatures of 350–380 K and a maximum at T = 450 K (Figure 5c).

The knowledge of storage modulus provides information about material stiffness. Figure 5a presents the E′ (T) plots of the NSSA and the NSSA/SG10 membranes. In comparison with the NSSA, a slight decrease in the storage modulus can be observed for the NSSA/SG10 sample. It may indicate the weaking of intermolecular bonds when 10 wt. % of SGS was added. As a result, the packing density in the polymeric matrix decreases. We

also observe the decrease in the difference of E′ values between both membranes as the temperature increases (Table 2).
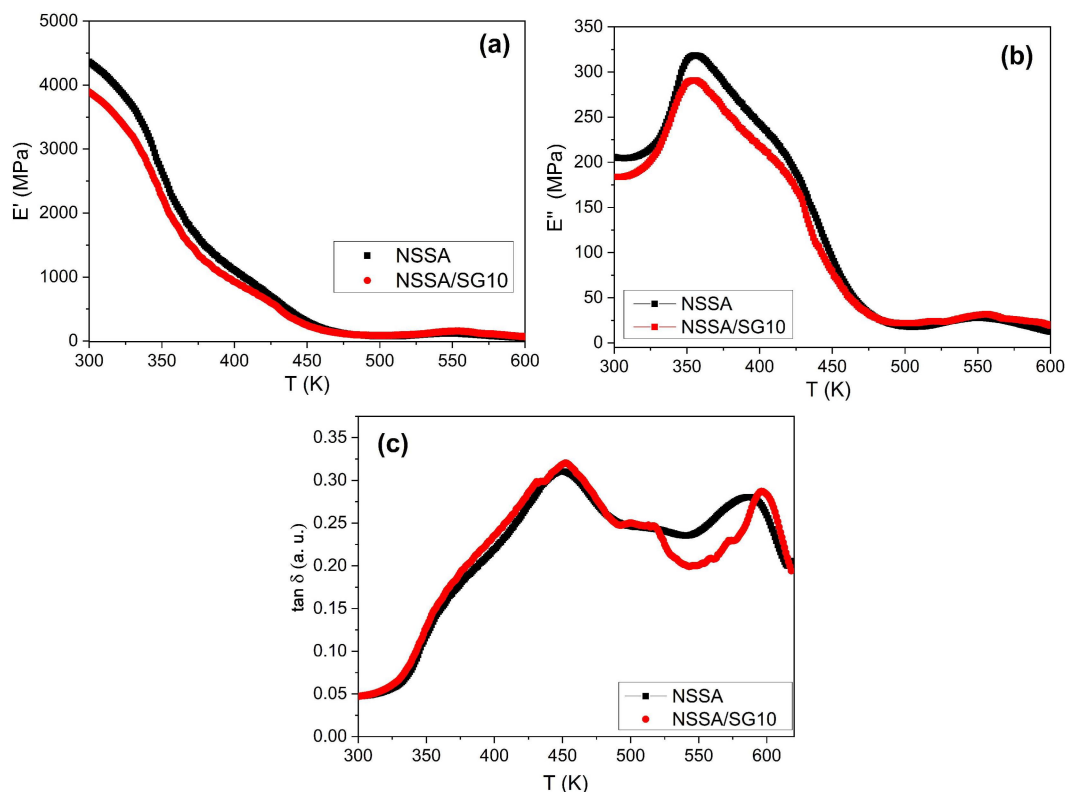

Figure 5. DMA curves of E′ (**a**), E″ (**b**) and tan δ (**c**) for NSSA and NSSA/SG10.

Table 2. Storage modulus of the NSSA and the NSSA/SG10 membranes.

Sample	E′, MPa		
	T = 298 K	T = 473 K	T = 573 K
NSSA	4390	130	85
NSSA/SG10	3940	122	115

Therefore, DMA studies showed that the relaxation behavior and elastic properties of the proton-conductive membranes do not change significantly by adding an inorganic component (silica) to their composition.

The large-scale commercialization of fuel cell technology needs higher power and current densities; unfortunately, at high operating current densities, the massive accumulation of water may cause flooding and prevent the diffusion of gases. It leads to the rapid degradation of PEMFC performance. Therefore, to achieve better fuel cell performance, it is crucial to improve water management. EIS is an important means to indicate the water behavior inside the cell.

The membrane conductivity is the main characteristic for a successful application in fuel cells. Therefore, its definition is a subject for further research.

Under the measurement conditions described in the "Characterization" Section above, both electrodes are symmetrical (made of the same metal composition) and can be considered reversible. In this case, the electrical conductivity of the membrane is defined as follows:

$$\sigma = \sigma_{el} + \sigma_i, \tag{4}$$

where σ_{el} is the electronic conductivity, and σ_i is the ionic conductivity.

In this case, the membrane should be considered both an ion conductor and an electronic insulator. Practically, the electronic conductivity is negligible ($\approx 10^{-9}$ Sm/cm) and should be neglected.

In general, the electronic conductivity should be at least five orders of magnitude lower than the ionic conductivity, i.e., the self-discharge current is below 10^{-5} the normal load current.

Electronic conductivity occurs due to the current of electrons (σ_e) and/or electron holes (σ_h):

$$\sigma_{el} = \sigma_e + \sigma_h. \tag{5}$$

The ionic conductivity of membranes is expected to arise solely from positively charged cations and negatively charged anions.

In the case in which the electrical conductivity measurements are conducted using an alternating current, the total resistance Z includes both real Z' and imaginary Z'' parts:

$$Z = Z' - jZ''. \tag{6}$$

By measuring the total resistance in the frequency range, we obtain the following:

$$Z(\omega) = Z'(\omega) - jZ''(\omega). \tag{7}$$

The test cell (Figure 1) included two electrodes in contact with the membrane, the conductivity of which we measured. The polymer/composite material acts as a resistor R_b connected in series with a double-layer capacitor C_{dl} at the interface and in parallel with the geometric capacitance C_q. Since the electrodes are not blocking, a transfer of electric charge (both electrons and holes) between the electrode and the ions in the membrane takes place. The kinetics of this process are not infinitesimally easy, and therefore, resistance R_{ct}, which indicates charge transfer, must be accounted for. Hence, on both interface sides, charge is accumulated, resulting in the creation of associated, significantly large charge transfer capacitance (C_{dl}) in parallel with the resistance (R_{ct}). An equivalent circuit for this case contains a resistor R_{ct} that shunts the double-layer capacitance (C_{dl}) (Figure 6). In this equivalent circuit, R_0 is an ohmic resistance.
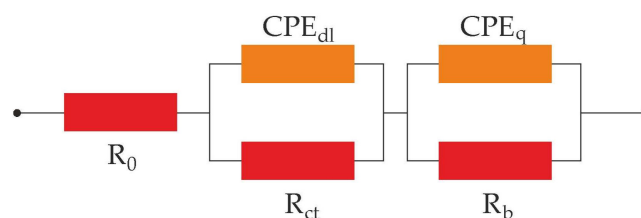

Figure 6. Equivalent scheme for the test cell.

Accepting this equivalent circuit, we obtain two semicircles on the Nyquist diagram: high-frequency semicircle, associated with bulk electrolyte, and low-frequency one, situated further from the origin of the coordinates, which reflects the processes at the electrode–membrane interface.

Considering experimentally measured Nyquist diagrams presented in Figure 7, we can see that the real hodograph has a slightly deformed two-arc dependence, and the center of the semicircles of which do not lie on the Z' axis. In this case, the capacitors C_{dl} and C_q must be replaced by constant phase elements CPE_{dl} and CPE_q, respectively. A constant-phase element can be considered as a hybrid between a resistor and a capacitor. This element is widely used for the impedance modeling of different electrochemical systems [27]. In our case, it displays a current flow in a spatially limited area with complex electrical conductivity. The impedance of an element including the constant phase should be described using following equation:

$$Z_{CPE} = \frac{1}{T(j\omega)^P} \quad (8)$$

where T is the proportionality coefficient, and $P = 0, 1, -1$ is the exponential factor that denotes the deviation phase.
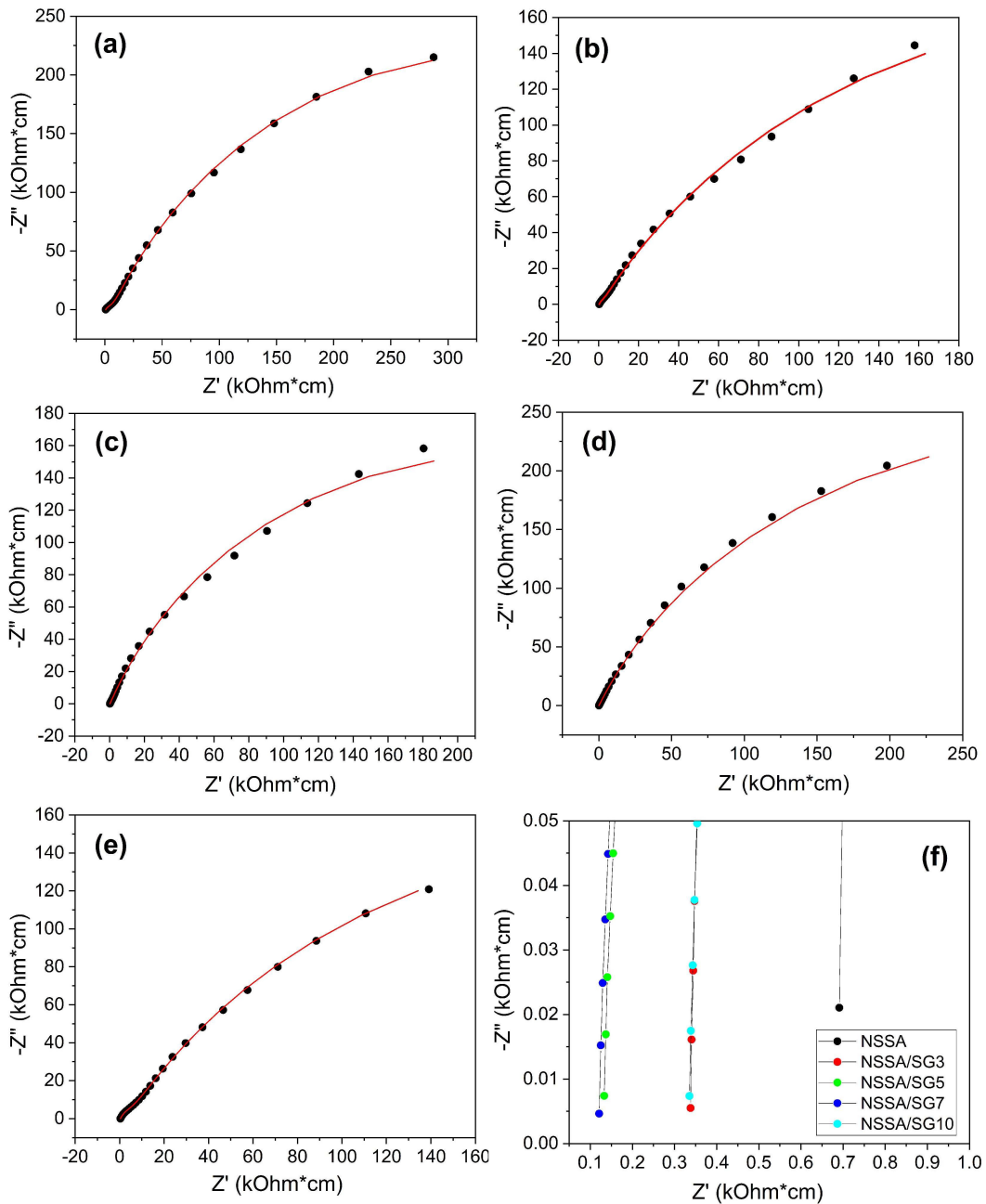

Figure 7. Nyquist plots for membranes: (**a**) NSSA; (**b**) NSSA/SG3; (**c**) NSSA/SG5; (**d**) NSSA/SG7; (**e**) NSSA/SG10; and (**f**) high-frequency part shown with high accuracy.

For integer p values, CPE is combined with classical elements that have lumped parameters R, C, and L, respectively. Accordingly, Table 3 generalizes parameters of the equivalent circuit elements for all investigated membranes, determined by simulation results. The modeling error did not exceed 5%.

Table 3. CPE and R_b values for the tested cells.

Sample	R_0, Ohm	CPE$_q$		R_b, Ohm	CPE$_{dl}$		R_{ct}, kOhm
		T, µF	P		T, µF	P	
NSSA	686.0	1.95	0.63	6085.0	2.66	0.72	680.0
NSSA/SG3	330.6	1.89	1.00	757.3	4.78	0.67	546.8
NSSA/SG5	133.1	0.47	1.00	39.5	4.03	0.76	457.1
NSSA/SG7	123.2	0.71	1.00	19.2	3.37	0.76	680.5
NSSA/SG10	333.1	2.93	0.86	3356.0	5.97	0.68	487.7

Proton conductivity values determined from the experimental data are presented in Table 4. The corresponding values were calculated for the highest frequency point. These values are inversely proportional to the R_0 values, taking into account the modeling error.

Table 4. Conductive parameters for the studied materials.

Sample	σ, mSm/cm	$\Delta\sigma$, mSm/cm
NSSA	1.45	0.04
NSSA/SG3	2.96	0.08
NSSA/SG5	7.52	0.20
NSSA/SG7	8.26	0.22
NSSA/SG10	2.99	0.08

The measured values of proton conductivity of the synthesized materials are 1.45–8.26×10^{-3} Sm/cm. It is observed that the values of proton conductivity of the hybrid composite materials gradually increase with the increase in the inorganic component content (from 2.96 ± 0.08 mSm/cm for the NSSA/SG3 membrane to 8.26 ± 0.22 mSm/cm for the NSSA/SG7 membrane) (Table 4).

If we look at the parameters of the low-frequency part of the impedance spectrum CPE$_{dl}$ and R_{ct}, we can see that the change in capacitance is within 55%, and the change in resistance is within 33%, respectively (Table 3). The largest change in the capacity of the CPE$_{dl}$ is observed with the addition of 3% silica nanoparticles, due to an increase in concentration of free charge carriers provided by added nanoparticles [28]. Also, as a result of the presence of silica nanoparticles, the resistance (R_{ct}) decreases due to the appearance of additional conductive contacts. It should be noted that the parameter P for CPE$_{dl}$ is in the range of 0.67–0.76, which indicates the heterogeneity of the formed double layer at the electrode–membrane interface. This can be caused by both the properties of the electrode–membrane interface itself and air presence, which was difficult to control under these conditions.

Much larger changes are observed in the high-frequency part of the impedance spectrum (Table 3). The corresponding parameters CPE$_q$ and R_b change several times and by several orders of magnitude. The introduction of silica nanoparticles formed using the sol–gel process of precursors leads to the expansion of pores and channels. Since channels that connect pores regulate the ion transport in membrane, its proton conductivity increases. However, with a further increase in the content of the inorganic component, we observed a sharp decrease in the value of the proton conductivity. At a high nanoparticle concentration, nanoparticles fill channels more densely, and accordingly, a decrease in proton conductivity takes place due to a decrease in pore space [29–32]. It should also be noted that the introduction of silica nanoparticles leads to the transition of the geometric capacity from CPE$_q$ to classical capacity, which is evidenced by the P parameter (Table 3), which is equal to 1.

According to the above considerations, comparing the values of resistance R_{ct} and resistance R_b, we can estimate the ratio of electronic to ionic conductivity in a given membrane. Thus, for the initial sample of NSSA, the difference is more than two orders of magnitude. After the addition of silica nanoparticles, the ratio increases significantly,

reaching a maximum value of 3.5×10^4 for NSSA/SG7. This indicates an increase in ionic conductivity relative to electronic conductivity due to the addition of silica nanoparticles.

As compared to the organic/inorganic membranes based on aliphatic monomers, the values of proton conductivity of the hybrid membranes including aromatic monomer are lower, and at the same time, the effect of the inorganic content on proton conductivity value is similar.

4. Conclusions

The proton-conductive organic/inorganic materials were synthesized by the UV curing of acrylic monomers and sodium styrene sulfonate with the simultaneous formation of nanoparticles in the sol–gel process. The content of the inorganic component was found to determine the properties of the obtained materials. The mass fractal organization, determined by SAXS, provides the sufficiently high level of proton transport, making the materials alternative candidates for PEMs in fuel cells. The introduction of silica to membrane structure does not lead to significant changes in its viscoelastic properties. However, as evidenced by impedance studies, it leads to the expansion of pores and the corresponding expansion of channels, which leads to an increase in proton conductivity. The subsequent increase in the silica nanoparticle concentration leads to the excessive sealing of the channels and thus to a decrease in conductivity.

The analysis of impedance spectra allows to construct a model of polarization and charge transfer for the membrane volume and the electrode–membrane interface. The model is presented in the form of an equivalent electrical circuit that adequately describes conduction processes.

To improve the performance of the fuel cell, the proposed approach needs to be developed. Since the conductivity value of the material is a consequence of its molecular structure, future research should include the effect of different fillers, in particular, the sol–gel systems of different compositions.

Author Contributions: Conceptualization, M.Z. and I.Y.; methodology, M.Z., F.I. and N.B.; software, M.Z. and P.C.; formal analysis, M.Z., O.D. and T.S.; investigation, M.Z., I.Y., F.I. and P.C.; data curation, M.Z., I.Y., F.I. and N.B; writing—original draft preparation M.Z. and I.Y.; writing—review and editing, M.Z., I.Y., F.I. and N.B.; visualization, M.Z., O.D. and P.C.; supervision, F.I.; funding acquisition, F.I. and P.C. All authors have read and agreed to the published version of the manuscript.

Informed Consent Statement: Informed consent was obtained from all subjects involved in the study.

Data Availability Statement: Data are contained within the article.

Conflicts of Interest: The authors declare no conflicts of interest.

References

1. Cigolotti, V.; Genovese, M.; Fragiacomo, P. Comprehensive Review on Fuel Cell Technology for Stationary Applications as Sustainable and Efficient Poly-Generation Energy Systems. *Energies* **2021**, *14*, 4963. [CrossRef]
2. Sharaf, O.Z.; Orhan, M.F. An overview of fuel cell technology: Fundamentals and applications. *Renew. Sustain. Energy Rev.* **2014**, *32*, 810–853. [CrossRef]
3. Sun, C.; Negro, E.; Vezzù, K.; Pagot, G.; Cavinato, G.; Nale, A.; Herve Bang, Y.; Di Noto, V. Hybrid inorganic-organic proton-conducting membranes based on SPEEK doped with WO₃ nanoparticles for application in vanadium redox flow batteries. *Electrochim. Acta* **2019**, *309*, 311–325. [CrossRef]
4. Zhang, Y. Chapter 12—Nanomembranes in fuel cells. In *Nanotechnology in Fuel Cells. Micro and Nano Technologies*; Elsevier: Amsterdam, The Netherlands, 2022; pp. 285–347. [CrossRef]
5. Purser, D.A. Chapter 2—Fire Safety Performance of Flame Retardants Compared with Toxic and Environmental Hazards. In *Polymer Green Flame Retardants*; Elsevier: Amsterdam, The Netherlands, 2014; pp. 45–86. [CrossRef]

6. Uosaki, K.; Okazaki, K.; Kita, H. Conductivity of Nation membranes at low temperatures. *J. Electroanal. Chem. Interfacial Electrochem.* **1990**, *287*, 163–169. [CrossRef]

7. Ozen, D.N.; Timurkutluk, B.; Altinisik, K. Effects of operation temperature and reactant gas humidity levels on performance of PEM fuel cells. *Renew. Sustain. Energy Rev.* **2016**, *59*, 1298–1306. [CrossRef]

8. Lohmann, R.; Cousins, I.T.; DeWitt, J.C.; Glüge, J.; Goldenman, G.; Herzke, D.; Lindstrom, A.B.; Miller, M.F.; Ng, C.A.; Patton, S.; et al. Are Fluoropolymers Really of Low Concern for Human and Environmental Health and Separate from Other PFAS? *Environ. Sci. Technol.* **2020**, *54*, 12820–12828. [CrossRef] [PubMed]

9. Gil, M.; Ji, X.; Li, X.; Na, H.; Hampsey, J.E.; Lu, Y. Direct synthesis of sulfonated aromatic poly (ether ether ketone) proton exchange membranes for fuel cell applications. *J. Membr. Sci.* **2004**, *234*, 75–81. [CrossRef]

10. Rafidah, R.S.R.; Rashmi, W.; Khalid, M.; Khalid, M.; Wong, W.Y.; Priyanka, J. Recent Progress in the Development of Aromatic Polymer-Based Proton Exchange Membranes for Fuel Cell Applications. *Polymers* **2020**, *12*, 1061. [CrossRef] [PubMed]

11. Zhang, Z.; Wu, L.; Xu, T. Novel aromatic proton-exchange polyelectrolytes via polyacylation of pre-sulfonated monomers. *J. Mater. Chem.* **2012**, *22*, 13996–14000. [CrossRef]

12. Rajangam, P.; Dharmalingam, S. Design of novel SPEEK-based proton exchange membranes by self-assembly method for fuel cells. *Ionics* **2013**, *19*, 1423–1436. [CrossRef]

13. Gao, S.; Xu, H.; Fang, Z.; Ouadah, A.; Chen, H.; Chen, X.; Shi, L.; Ma, B.; Jing, C.; Zhu, C. Highly sulfonated poly (ether ether ketone) grafted on graphene oxide as nanohybrid proton exchange membrane applied in fuel cells. *Electrochim. Acta* **2018**, *283*, 428–437. [CrossRef]

14. Jun, M.-S.; Choi, Y.-W.; Kim, J.-D. Solvent casting effects of sulfonated poly (ether ether ketone) for Polymer electrolyte membrane fuel cell. *J. Membr. Sci.* **2012**, *396*, 32–37. [CrossRef]

15. Mabrouk, W.; Ogier, L.; Vidal, S.; Sollogoub, C.; Matouss, F.; Fauvarque, J.F. Ion exchange membranes based upon crosslinked sulfonated polyethersulfone for electrochemical applications. *J. Membr. Sci.* **2014**, *452*, 263–270. [CrossRef]

16. Matsushita, S.; Kim, J.-D. Organic solvent-free preparation of electrolyte membranes with high proton conductivity using aromatic hydrocarbon polymers and small cross-linker molecules. *Solid State Ion.* **2018**, *316*, 102–109. [CrossRef]

17. Klein, L.C. Sol-Gel Process for Proton Exchange Membranes. *Key Eng. Mater.* **2008**, *391*, 159–168. [CrossRef]

18. Heimerdinger, P.; Rosin, A.; Danzer, M.A.; Gerdes, T. A Novel Method for Humidity-Dependent Through-Plane Impedance Measurement for Proton Conducting Polymer Membranes. *Membranes* **2019**, *9*, 62. [CrossRef]

19. Müller, F.; Ferreira, C.A.; Azambuja, D.S.; Alemán, C.; Armelin, E. Measuring the proton conductivity of ion-exchange membranes using electrochemical impedance spectroscopy and through-plane cell. *J. Phys. Chem. B* **2014**, *118*, 1102–1112. [CrossRef] [PubMed]

20. Cooper, K.R. Progress toward Accurate Through-Plane Ion Transport Resistance Measurement of Thin Solid Electrolytes. *J. Electrochem. Soc.* **2010**, *157*, B1731–B1739. [CrossRef]

21. Di Noto, V.; Vezzù, K.; Crivellaro, G.; Pagot, G.; Sun, C.; Meda, L.; Rutkowska, I.A.; Kulesza, P.J.; Zawodzinski, T.A. A general electrochemical formalism for vanadium redox flow batteries. *Electrochim. Acta* **2022**, *408*, 139937. [CrossRef]

22. Sun, C.; Negro, E.; Nale, A.; Pagot, G.; Vezzù, K.; Zawodzinski, T.A.; Meda, L.; Gambaro, C.; Di Noto, V. An efficient barrier toward vanadium crossover in redox flow batteries: The bilayer [Nafion/(WO$_3$)x] hybrid inorganic-organic membrane. *Electrochim. Acta* **2021**, *378*, 138133. [CrossRef]

23. Yuan, X.; Wang, H.; Sun, J.C.; Zhang, J. AC impedance technique in PEM fuel cell diagnosis—A review. *Int. J. Hydrogen Energy* **2007**, *32*, 4365–4380. [CrossRef]

24. Zhyhailo, M.; Demchyna, O.; Yevchuk, I.; Makota, O. Co(II) and Ni(II) Removal from Aqueous Solutions by Polymer and Polymer/Silica Adsorbents with Sulfo and Carboxyl groups. *Acta Chim. Slov.* **2023**, *70*, 361–370. [CrossRef]

25. Zhyhailo, M.; Horechyy, A.; Meier-Haack, J.; Formanek, P.; Malanin, M.; Arnhold, K.; Schneider, K.; Yevchuk, I.; Fery, A. Proton conductive membranes from covalently cross-linked poly(acrylate)/silica interpenetrating networks. *Macromol. Mater. Eng.* **2021**, *306*, 2000776. [CrossRef]

26. Zheltonozhskaya, T.; Shembel, E.; Fedorchuk, S.; Kunitskaya, L.; Maksyuta, I.; Permyakova, N.; Gomza, Y. Nanostructured triblock copolymers with chemically complementary components and their ionic conductivity. *J. Res. Updates Polym. Sci.* **2013**, *1*, 84–95. [CrossRef]

27. Barsoukov, E.; Macdonald, J.R. (Eds.) *Impedance Spectroscopy Theory, Experiment, and Applications*; John Wiley & Sons, Inc.: Hoboken, NJ, USA, 2005; 595p.

28. Olenych, I.B.; Aksimentyeva, O.I.; Horbenko, Y.Y.; Tsizh, B.R. Electrical and sensory properties of silicon–graphene nanosystems. *Appl. Nanosci.* **2021**, *12*, 579–584. [CrossRef]

29. Zhyhailo, M.; Demchyna, O.; Rymsha, K.; Yevchuk, I.; Rachiy, B.; Kochubey, V. Proton Conductive Organic-Inorganic Nanocomposite Membranes Derived by Sol-Gel Method. *Chem. Chem. Technol.* **2019**, *13*, 436–443. [CrossRef]

30. Vyas, M.K.; Chandra, A. Ion–Electron-Conducting Polymer Composites: Promising Electromagnetic Interference Shielding Material. *ACS Appl. Mater. Interfaces* **2016**, *8*, 18450–18461. [CrossRef]

31. Tanga, X.; Zhanga, Y.; Xu, S. Temperature sensitivity characteristics of PEM fuel cell and output performance improvement based on optimal active temperature control. *Int. J. Heat Mass Transf.* **2023**, *206*, 123966. [CrossRef]

32. Yan, S.; Yang, M.; Sun, C.; Xu, S. Liquid Water Characteristics in the Compressed Gradient Porosity Gas Diffusion Layer of Proton Exchange Membrane Fuel Cells Using the Lattice Boltzmann Method. *Energies* **2023**, *16*, 6010. [CrossRef]